

UC San Diego

UC San Diego Previously Published Works

Title

Organic Upconversion Imager with Dual Electronic and Optical Readouts for Shortwave Infrared Light Detection

Permalink

<https://escholarship.org/uc/item/5rd5n50v>

Journal

ADVANCED FUNCTIONAL MATERIALS, 31(16)

ISSN

1616-301X

Authors

Li, Ning
Eedugurala, Naresh
Leem, Dong-Seok
[et al.](#)

Publication Date

2021

DOI

10.1002/adfm.202100565

Peer reviewed

Organic Upconversion Imager with Dual Electronic and Optical Readouts for Shortwave Infrared Light Detection

Ning Li, Naresh Eedugurala, Dong-Seok Leem, Jason D. Azoulay, and Tse Nga Ng*

There remains a critical need for large-area imaging technologies that operate in the shortwave infrared spectral region. Upconversion imagers that combine photo-sensing and display in a compact structure are attractive since they avoid the costly and complex process of pixilation. However, upconversion device research is primarily focused on the optical output, while electronic signals from the imager remain underutilized. Here, an organic upconversion imager that is efficient in both optical and electronic readouts, extending the capability of human and machine vision to 1400 nm, is designed and demonstrated. The imager structure incorporates interfacial layers to suppress non-radiative recombination and provide enhanced optical upconversion efficiency and electronic detectivity. The photoresponse is comparable to state-of-the-art organic infrared photodiodes exhibiting a high external quantum efficiency of $\leq 35\%$ at a low bias of ≤ 3 V and 3 dB bandwidth of 10 kHz. The large active area of 2 cm² enables demonstrations such as object inspection, imaging through smog, and concurrent recording of blood vessel location and blood flow pulses. These examples showcase the potential of the authors' dual-readout imager to directly upconvert infrared light for human visual perception and simultaneously yield electronic signals for automated monitoring applications.

SWIR photodetector working in conjunction with a visible light-emitting diode.^[8] Low energy SWIR photons absorbed in the detection layer are locally upconverted into high energy photons at the emissive layer, providing a visible image of the incident infrared pattern. The direct upconversion process allows the imager to be pixel-less; that is, it does not rely on pixelated backplanes to register spatial variations of the incoming SWIR light. Upconversion imagers combine photo-sensing and display functions in a single compact structure; thus, they are under rapid development toward the realization of economical, large-area SWIR imagers.

Prior work on upconversion imagers utilized III–V compound semiconductors within the photo-sensing layers,^[9,10] but the fast lateral charge diffusion inherent to these materials results in poor image resolution. Solution-processable materials such as colloidal quantum dots (CQD)^[11,12] and organic semiconductors^[13–19] have improved spatial resolution by virtue of

Imaging in the shortwave infrared (SWIR, wavelength λ of 1–3 μm) plays a critical role in diverse fields ranging from biomedical imaging to industrial and environmental monitoring.^[1–7] However, SWIR imaging technologies are limited by the complex and costly integration of SWIR sensing elements with the readout integrated circuits (ROIC). An alternate approach that circumvents the need for ROIC pixilation is based on upconversion imaging devices, which consist of a


their lower lateral conductivity. Consequently, this work examines solution-processable polymers^[20–28] for infrared sensing, leveraging their amorphous nature to form smooth thin films that result in high quality and uniform optical emission. This enables the fabrication of a large-area organic imager with dimensions of 2 cm², indicative of the scalability toward technologies such as wide-field imaging for navigation or lab-on-a-chip applications.^[29]

To date, research on upconversion imagers has principally emphasized the optical output, with the upconversion efficiency and spatial resolution as main performance metrics. While the optical readout is certainly important for human visual perception, obtaining an electronic readout is necessary for implementing machine vision and signal processing algorithms.^[30,31] To achieve this, previous efforts employed an indirect approach where the visible output of an upconversion imager was captured using a conventional camera in order to record an electronic signal. In this work, we engineered our imagers to provide direct and efficient electronic signals without an external camera, thereby simplifying the electronic readout. While this approach limits the spatial information in the electronic signal when compared to ROIC-based architectures, our upconversion imager is significantly more straightforward to fabricate and offers a format that is easier to scale to large-area than conventional ROIC systems.

Dr. N. Li, Prof. T. N. Ng
Department of Electrical and Computer Engineering
University of California San Diego
9500 Gilman Drive, La Jolla, CA 92093-0407, USA
E-mail: tnn046@ucsd.edu

Dr. N. Eedugurala, Prof. J. D. Azoulay
School of Polymer Science and Engineering
University of Southern Mississippi
118 College Drive #5050, Hattiesburg, MS 39406, USA

Dr. D.-S. Leem
Samsung Advanced Institute of Technology (SAIT)
Samsung Electronics Co., Ltd.
130 Samsung-ro, Yeongtong-gu, Suwon-si, Gyeonggi-do 16678, South Korea

 The ORCID identification number(s) for the author(s) of this article can be found under <https://doi.org/10.1002/adfm.202100565>.

DOI: 10.1002/adfm.202100565

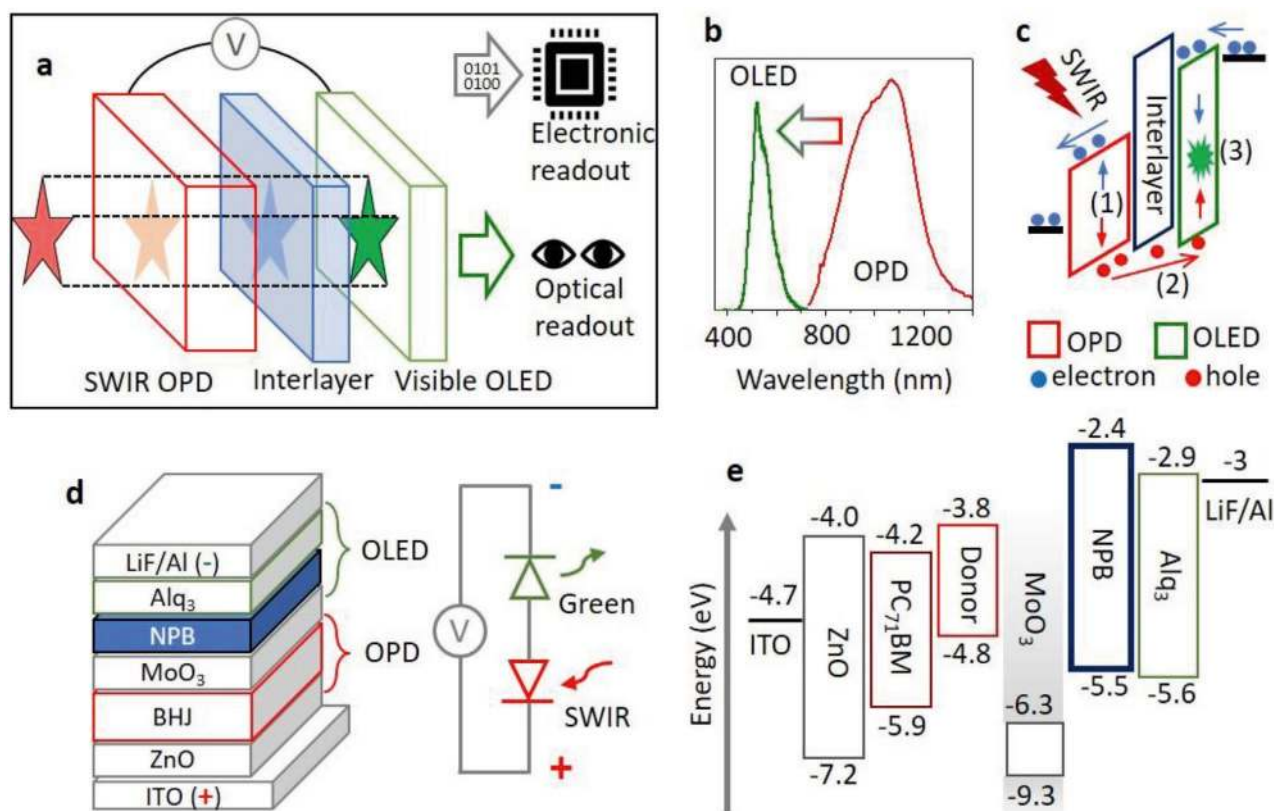


Figure 1. Design of the dual-readout imager. a) A schematic of the upconversion imager with dual electronic and optical readouts. b) The absorption spectrum of the SWIR OPD (red line) and the emission spectrum of the visible OLED (green line). c) An illustration of photogeneration (1), charge transport (2), and radiative recombination (3) processes in the device. d) Material stacks of the imager, along with the equivalent circuit model. e) An energy level diagram for the materials in the imager.

To enable the novel use of an upconversion imager to deliver dual electronic and optical readouts (Figure 1a), the imager design incorporated interfacial layers with proper energy levels that suppress non-radiative recombination. The effect of these layers in relation to the device current and upconversion efficiency offer insight into design guidelines for interfacial layers to improve electronic and optical outputs. We also compared the electronic photoresponse of the organic upconversion imager to a prototypical SWIR organic photodiode (OPD). The upconversion imager demonstrated comparable performance to the SWIR OPD in both speed and detectivity, with a broadband response from 800 to 1400 nm and a high external quantum efficiency (EQE) of $\leq 35\%$ at a low bias of ≤ 3 V. This level of performance enabled successful SWIR visualization related to object inspection, imaging through smog, and the synergistic recording of blood vessel vasculature location and blood flow pulses. The last example showcased the capability of dual electronic and optical readouts, in which the imager signals can be readily viewed by people and integrated with machine vision systems to meet the increasing demand associated with automated monitoring.

1. Design of the Dual-Readout Upconversion Imager

The upconversion imagers in this report are tandem devices combining a SWIR OPD and visible organic light-emitting

diode (OLED). In Figure 1b, the absorption of the OPD layer spans wavelengths from 800 to 1400 nm, which is state-of-the-art for organic upconversion imagers. The visible output of the OLED corresponds to the green spectral region in which human vision is most sensitive. As shown in Figure 1c, the working mechanism of the upconversion imager involves multiple steps. In step 1, excitons generated by SWIR photons are separated to yield free electrons and holes. In step 2, electrons are extracted at the anode, and holes are transported into the emissive layer. In step 3, the holes injected into the emissive layer recombine with electrons injected at the cathode, generating a visible photon. The visible image retains the same pattern as the incoming SWIR light, as a result of the weak lateral transport in the organic semiconductor.

The upconversion process in this imager is based on electronic transport, using the SWIR photodiode to control the charge injection into the OLED. While in optics, upconversion refers to an anti-Stokes type emission where two or more low-energy photons are absorbed, giving rise to the emission of photons with higher energy. The optical upconversion takes place through mechanisms like triplet-triplet annihilation, energy-transfer upconversion, and excited-state absorption. The structure here does not operate in the sense of optical anti-Stokes upconversion, but it works through device engineering of the back-to-back diodes.

The specific layers comprising the device structure are shown in Figure 1d, along with the equivalent circuit model illustrating that the OPD and OLED layers are integrated in a back-to-back diode (n-p-n) configuration. The visible OLED is forward biased while the SWIR OPD is reverse biased. The OPD is a bulk heterojunction (BHJ) consisting of a SWIR-sensitive polymer^[32–35] and a fullerene derivative^[36] whose chemical structures can be found in Figure S1a, Supporting Information. Figure 1e presents the lowest unoccupied molecular orbital (LUMO) and highest occupied molecular orbital (HOMO) levels of each material. *N,N'*-bis(naphthalen-1-yl)-*N,N'*-bis(phenyl)benzidine (NPB) serves as an electron-blocking layer that confines electrons inside the emissive tris(8-hydroxyquinoline)aluminum(III) (Alq₃) layer. The energy levels of molybdenum oxide (MoO₃)^[37] and NPB are matched to the donor polymer and Alq₃. This ensures an energetically favorable transport route for photogenerated holes from the BHJ to the emissive

Alq₃ layer. Below, we compare the performance of devices with and without the NPB layer, in order to examine how the interlayer affects non-radiative recombination and also pinpoint criteria relevant to enhancing imager outputs.

2. Effect of the Interlayer on the Electronic and Optical Readouts

Figure 2a shows the current density–voltage characteristics of the upconversion imagers with and without the NPB layer. For the imager incorporating NPB, a lower dark current density was measured and the corresponding photoresponse was higher than the device without NPB. The ratio between the current under illumination with respect to the dark is at least two times higher when NPB is present in the upconversion imager. Figure 2b shows the EQE as a function of incident

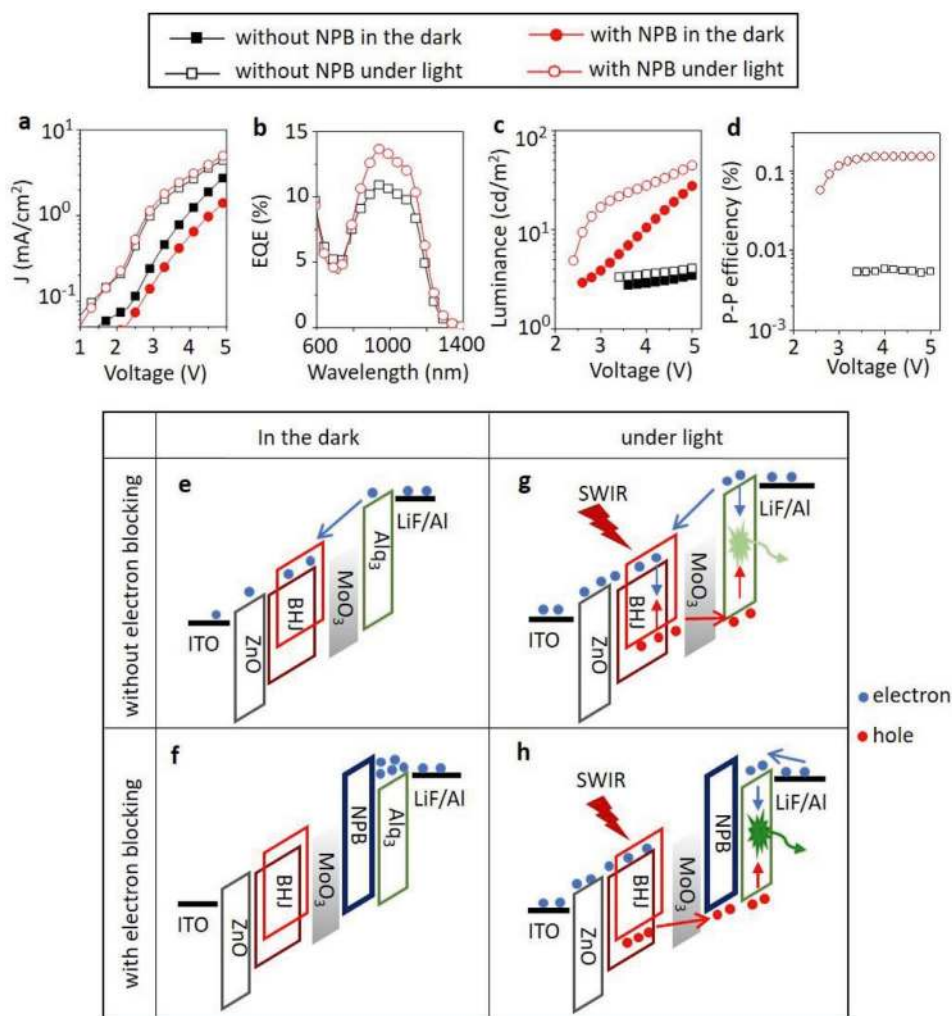


Figure 2. Effect of the NPB layer on electronic and optical readouts of the dual-readout imager, in the dark and under illumination. The incident light source wavelength was 1050 nm at an intensity of 4.2 mW cm⁻². a) Current densities versus applied bias. b) EQE at a bias of 3 V versus incident wavelength. c) Luminance of the OLED in the imager versus applied bias. d) SWIR photon-to-visible photon upconversion efficiency versus applied bias. e–h) Illustrations comparing charge transport and recombination processes for imagers with and without the NPB interfacial layer. The illustrations depict the charge dynamics at low applied bias assuming no hole injection from the anode. The NPB blocks electron transport, reducing dark current and facilitating radiative recombination in Alq₃ in order to increase emission efficiency.

wavelength extracted from the photocurrent, which is defined as the device current under illumination subtracted by the dark current (see Experimental Section for full details). Across all wavelengths measured, the imager with NPB exhibited a higher EQE than the one without NPB.

Similar to the electronic response, the optical output of the imager was improved by incorporating an NPB layer in the structure. The luminance in Figure 2c and the SWIR photon-to-visible photon upconversion efficiency η_{p-p} in Figure 2d were more than one order of magnitude higher in the imager with NPB. For the upconversion device with NPB, hole injection was sufficiently blocked at a low bias of <3 V. But when the voltage is increased to >3 V, hole injection from indium tin oxide (ITO)/zinc oxide (ZnO) side increased, resulting in visible light emission even when there was no incident SWIR light on OPD. Then the luminance ratio decreased, as shown in Figure S2, Supporting Information. The optimal bias was around 3 V to maximize the imaging contrast. As for the lateral resolution of the imager, charge carrier mobility and exciton/charge diffusion length would affect the image sharpness. With increasing electric field, charges were collected faster such that there would be less time for lateral diffusion, which would improve the spatial resolution.

Details of the η_{p-p} measurement and calculations can be found in the Experimental Section. The upconversion efficiency can be approximated by the product of the detector EQE and emitter efficiency ($\text{EQE}_{\text{emitter}}$), $\eta_{p-p} \approx \text{EQE}_{\text{detector}} \times \text{EQE}_{\text{emitter}}$. From this approximation, we can infer that η_{p-p} in our devices was limited by $\text{EQE}_{\text{emitter}}$. While the minimum detector efficiency was at least $\approx 15\%$, the emitter efficiency was only $\approx 1\%$. An upconversion efficiency of 0.15% was measured at a 3 V bias in the imager with NPB. While this efficiency has room for improvement, it exceeds other upconversion imagers based on organic material systems^[11,13] and provides the unique capability of sensing beyond 1 μm , particularly for sensing beyond the near-infrared since prior organic imagers were limited to $\lambda < 1 \mu\text{m}$.

Inserting the NPB layer between the OPD and OLED segments raises the device photocurrent and upconversion efficiency of the imager. A high dark current was observed without NPB, due to electron transport from the cathode to the anode (Figure 2e). The dark current was reduced upon incorporating the NPB layer because the LUMO level of NPB blocked electron injection into the BHJ (Figure 2f). Under illumination, the electron-blocking property of NPB played a critical role in reducing non-radiative recombination. Without the NPB layer, injected electrons were transported to the SWIR BHJ where they recombined with photogenerated holes. This non-radiative recombination was detrimental to upconversion, resulting in weak luminance from the imager (Figure 2g). Alternatively, with the NPB blocking layer, injected electrons were confined to the Alq₃ emissive layer. This configuration in Figure 2h promoted radiative recombination of photogenerated holes and injected electrons within the emissive layer, increasing the device luminance and upconversion efficiency.

We note that prior work^[8] has used blocking layers to tune the radiative recombination zone in upconversion imagers. Here, we demonstrate another benefit of the NPB blocking layer, in which it minimizes the loss of photogenerated charges

due to non-radiative recombination in the BHJ. In theory, the electronic readout should be an intrinsic function by the nature of stacking OPD/OLED—if we consider the OLED as a regular non-emitting diode, then it would be an OPD/diode switch structure commonly used in active matrix electronic readout pixels. However, in practice, without a proper design of the interlayer, either the electronic or the optical readout is not efficient. This is because, in the upconversion device, the operation of OPD and OLED are coupled and without metal electrodes in between, unlike individual OPDs/diodes in matrix pixels. The NPB layer was instrumental in increasing the signal-to-noise metric in our upconversion imagers for delivering a sensitive electronic readout as detailed below.

3. Analysis of the Electronic Readout in the Upconversion Imager

Under SWIR illumination, the imager current increased due to the photogeneration of additional carriers. We compared the current response of the imager with NPB to a typical OPD, in order to examine how the imager tandem structure impacted electronic performance in comparison to a single photodiode. The OPD structure is shown in Figure S1b, Supporting Information. Figure 3a presents the device EQE as a function of incident light intensity. Both the imager and the OPD showed higher EQE with decreasing light intensity, since recombination was reduced at low carrier densities. At an applied bias of 3 V, the imager EQE increased to 35%, slightly lower than the OPD (EQE < 40%). For the dark current measured at equivalent electric fields,^[38–40] the imager exhibited less noise than the OPD (Figure 3b). The EQE and noise characteristics taken together determined the specific detectivities D^* shown in Figure 3c. The equation for D^* is listed in the Experimental Section, and the peak D^* reached 3.8×10^9 Jones. While the signal is slightly lower in the imager than the OPD, the noise is much smaller in the imager than the OPD. In the end, due to the denominator in the signal-to-noise ratio (SNR), the imager shows higher SNR and D^* than the OPD.

The detectivities of the individual OPD and the upconversion imager were obtained by measuring the current spectral densities through a spectrum analyzer.^[38] The SNRs are shown in Figure 3d as different light powers were shone on the device. The incident power was decreased to determine the noise equivalent power (NEP) when the signal amplitude reached the noise floor, as illustrated in Figure 3d inset and shown with details in Figure S3, Supporting Information. For the 940 nm illumination modulated at 313 Hz, the minimum detectable power when SNR = 1 is 0.15 nW for SWIR PD and 0.11 nW for the imager, measured with a light input bandwidth frequency of 2 Hz. The resulting NEPs are $10^{-10} \text{ W Hz}^{-0.5}$ for the SWIR OPD and $7.8 \times 10^{-11} \text{ W Hz}^{-0.5}$ for the imager, respectively. From the NEP values, the detectivities were determined to be 3×10^9 Jones for the SWIR PD and 3.8×10^9 Jones for the imager. Actually this comparison points out a new way to improve individual SWIR OPDs by including NPB blocking layers, as they are shown to be effective in the upconversion structures.

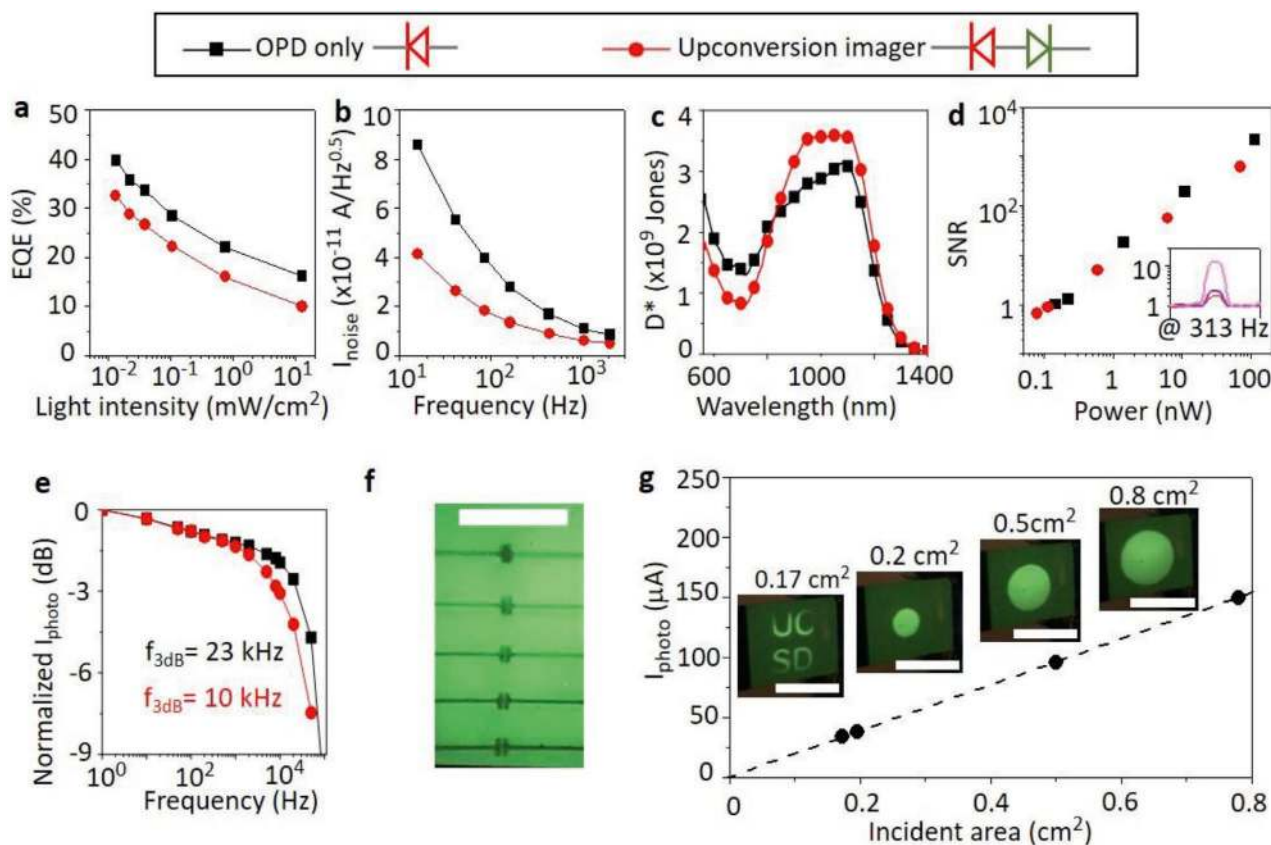


Figure 3. Comparison of the response from a SWIR photodiode and a dual-readout imager. a) EQE versus incident light intensity at a wavelength of 1050 nm. b) Noise current versus frequency. c) Specific detectivity versus wavelength of incident light. d) Signal-to-noise ratio (SNR) as a function of incident light power at a wavelength of 940 nm. Inset: SNR peak with the incident light modulated at 313 Hz, as the incident power decreased from 0.6 nW (light purple line) to 0.08 nW (dark purple line). e) Normalized photocurrent versus modulation frequency. f) Spatial resolution determined by imaging channel gaps of 45, 60, 75, 90, and 120 μm , from top to bottom. The scale bar is 5 mm. g) Photocurrent of the upconversion imager as a function of the incident light area, at a fixed light intensity of $\approx 10 \text{ mW cm}^{-2}$ at $\lambda = 940 \text{ nm}$. The photographs are visible images emitted by the imager from upconverting incident SWIR light, scale bars are 1 cm. In these measurements, the SWIR OPD was reverse biased at 1.5 V, and the imager was biased at 3 V. This accounts for differences in thickness and ensures operation at a similar electric field as the OPD. The active areas are the same for the OPD and upconversion imager, at 0.1 cm^2 for parts (a–e) and 2 cm^2 for parts (f,g).

The incident light intensity in the photon-to-photon upconversion measurements was 4.2 mW cm^{-2} in Figure 2a–d, and there remained an optical contrast of around 4 as shown in Figure S2, Supporting Information. Therefore, the minimum detectable level of light intensity was on the order of 1 mW cm^{-2} for the optical readout. Whereas for the electronic readout, the NEP is the lowest light power that can be distinguished by the detector. As discussed above, the NEP of the imager was measured to be $7.8 \times 10^{-11} \text{ W Hz}^{-0.5}$, several orders of magnitude better than that of the optical readout, indicating the high sensitivity of the electronic response.

The temporal response of the devices was measured using light pulses modulated at frequencies from 1–50 kHz as shown in Figure 3e. The 3 dB bandwidths measured for the imager and OPD were 10 and 23 kHz, respectively. The photocurrent rise and fall characteristics and the device impedance are shown in Figure S4, Supporting Information. The measured shunt resistance was higher (nearly triple) in the imager when compared to the OPD, on account of the presence of more resistive layers in the imager. The total resistance-capacitance

time constant was larger and led to a longer response time in the imager as compared to the OPD.

The tandem imager maintained similar electronic performance as a single OPD while adding the advantage of SWIR visualization. Upconversion by the imager showed uniform visible emission over the entire 2 cm^2 active area, as shown in Figure S5, Supporting Information. For optical readout, the spatial resolution of the imager was determined by imaging narrow channels of a transistor mask. Channel gaps of 45, 60, 75, 90, and 120 μm were imaged, as shown in Figure 3f. Channel length of 60 μm is readily resolved in the upconversion image, corresponding to a resolution of ≈ 423 pixels per inch, which is better than pixelated organic imagers.^[41,42]

Regarding the limitation of the electronic readout, our pixelless imager is averaging out spatial information in the electrical signal. However, some spatial information can be inferred based on the relationship that the photocurrent from the large-area imager depended on the incident light power P_{in} and the exposure area A' , as $I_{\text{photo}}(P_{\text{in}}, A')$. Using a fixed incident light power, we measured the photocurrent as a function of

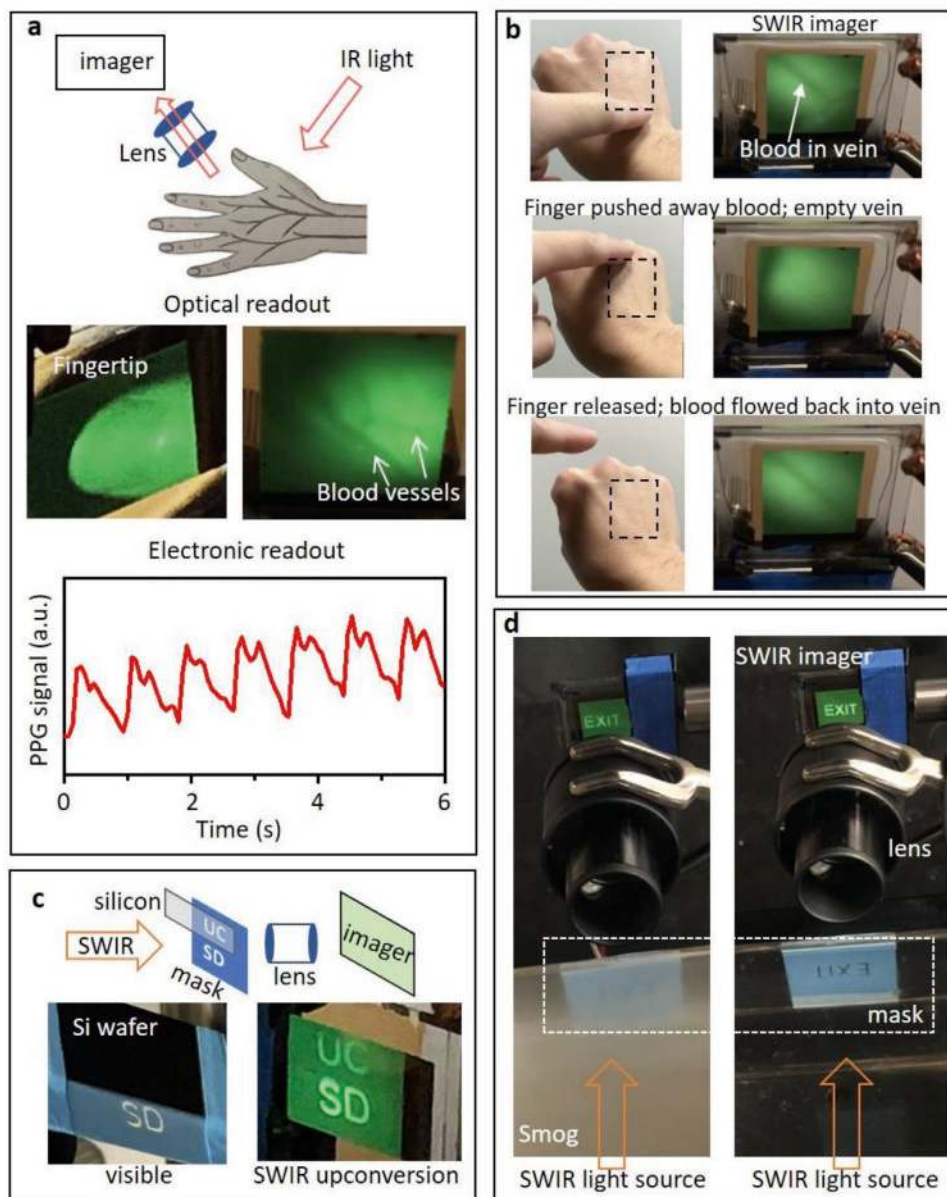


Figure 4. Imaging capabilities of the dual-readout imager. a) The reflected IR light from a human hand was upconverted by the imager, showing fingertip and blood vessel features. Simultaneously, without the need of skin contact, the imager captured the photocurrent modulation corresponding to a photoplethysmogram (PPG) of a person's heartbeats. b) Imaging blood flow in a vein. The dashed box indicates the area being imaged. Real-time movie is provided in Video S2, Supporting Information. c) Imaging of an object behind a silicon wafer. The mask was partially covered by silicon which was opaque to visible light but transmitted SWIR, revealing the letters under the silicon wafer. d) Imaging through a smog chamber. Without smog, the "EXIT" mask was discernable (right); but with smog, visible light was strongly scattered and the mask letters were obscured in the visible (left). As a result of the weak scattering of SWIR light by smog, the upconversion imager was able to capture the mask pattern and clearly displayed the "EXIT" letters. The path length of the smog chamber was 10 cm. The imager active area was 2 cm² at an applied bias of 3 V.

exposure area in Figure 3g. The SWIR illumination patterns were adjusted by masks with different cut-out areas and the upconversion images associated with the different masks are shown in the inset photographs in Figure 3g. The photocurrent was linearly proportional to the area exposed to SWIR light. As such, changes in current can be used to estimate the size of objects passing between the light source and the imager, which is useful for automated inspection applications.

4. Imaging Applications using the Dual-Readout Imager

In Figure 4a, SWIR light was shone onto a person's hand and the reflected light was upconverted by the imager. The resulting image showed details of the finger tip, such as the cuticle and the white edge of the fingernail. The imager was also used to locate blood vessels in the hand (Videos S1 and S2,

Supporting Information), relevant for biometric authentication through vasculature patterns. The blood vessels were darker in color compared to the background, because of the absorption of SWIR light by the blood flowing inside. Figure 4b shows a motion sequence of manipulating blood flow, as one pressed down on a vein to push away blood and then released the pressure to let blood flow back into the vein. The dynamic demonstration is provided in Video S2, Supporting Information.

During the mapping of blood vessels, the imager simultaneously captured the periodic change in reflected SWIR light intensity arising from the pulsating nature of the blood flow inside the body. This modulation in photocurrent in Figure 4a, known as a photoplethysmogram (PPG),^[43,44] originated from heart beats pumping blood which changed the SWIR absorption of the tissue. The measured waveform showed clear systolic and diastolic phases, and the heart rate was calculated to be ≈ 70 beats per minute. Prior PPG sensors^[5,21,43–45] required direct contact to human skin in order to detect the systolic and diastolic characteristics. Here, in Figure 4a, the photocurrent was recorded with no physical contact between the detector and the subject, while clearly displaying all the PPG fine features and offering the advantage of non-contact measurements, which can be easier to deploy and more comfortable for the subject. From these demonstrations, the dual-readout upconversion imager allowed non-contact spatio-temporal recording of PPG and blood vessel mapping, presenting strong potential for biomedical studies and biometric applications.

The upconversion imager was also used to demonstrate the advantages of using SWIR light for inspection or environmental monitoring in complement with visible light. Specifically, electronic foundries often require inspection through silicon, which are opaque in the visible but allow significant transmission for $\lambda > 1.1 \mu\text{m}$. As shown in Figure 4c, SWIR light is suitable for imaging through silicon, where the mask pattern (the letters “UC”) covered by a silicon wafer were clearly revealed by the SWIR imager. Another example in Figure 4d compared the effect of smog on visible versus SWIR imaging, since the need to image through smog has grown in importance for wildfire control and environmental safety. Visible light was strongly scattered by smog, and it was difficult to identify the letters (EXIT) on the mask through the smog chamber. On the other hand, SWIR light penetrated the smog so that the “EXIT” mask was unambiguously visualized by the upconversion imager.

We summarize the performance of prior upconversion imagers for comparison to our device in Table S1, Supporting Information. Most of the prior works on organic semiconductors were limited to near-infrared wavelengths below 1100 nm.^[8,14–19] The spectral range was extended into SWIR by using CQD in the detector layer, and the state-of-the-art CQD device showed an upconversion efficiency $\eta_{\text{p-p}}$ of 6.5% at 10 V.^[11] However, CQD materials such as lead sulfide/selenide are toxic to human health and place restrictions on applications. In this work we chose to use organic SWIR materials which do not pose toxicity risks. In the category of organic upconversion imagers, the record $\eta_{\text{p-p}}$ was 0.1% at 14 V.^[13] By comparison, our device here reached $\eta_{\text{p-p}} = 0.15\%$ at a low operating voltage of 3 V, and the active imaging area is 2 cm², larger than the 0.05 cm² area in CQD imagers.

5. Conclusions

This work presented the design of a large-area organic upconversion imager that offered efficient electronic and optical dual-readouts to detect infrared radiation out to 1400 nm. The key to improving efficiency resulted from the incorporation of an interlayer that suppressed non-radiative recombination. For the materials system here, the NPB interlayer blocked electron injection into the OPD and reduced dark current noise and minimized the loss of photogenerated holes. The interlayer enhanced upconversion efficiency by facilitating radiative recombination within the emissive OLED layer. Furthermore, the imager delivered an electronic photoresponse comparable to typical OPDs and was unaffected by extra layers in the tandem structure, enabling a compact display for instantaneous SWIR visualization. Our large-area imager allowed object size estimation relevant to industrial or environmental monitoring. Furthermore, non-contact measurements were enabled that allowed the tracking of physiological heartbeat from a human hand from the photocurrent while presenting optical images of the tissue sample. This dual-readout imager is simple and economical to fabricate and attractive for extending the utility of SWIR imaging to both human visualization and machine vision.

6. Experimental Section

Material Preparation: All the chemicals were used as received without further purification. For the SWIR BHJ, the donor polymer poly(4-(5-(4-(3,5-bis(dodecyloxy)benzylidene)-4H-cyclopenta[2,1-b:3,4-b']dithiophen-2-yl)thiophen-2-yl)-6,7-dioctyl-9-(thiophen-2-yl)-[1,2,5]thiadiazolo[3,4-g]quinoxaline)^[32] was blended with the fullerene derivative acceptor PC₇₁BM (Ossila Ltd.) at a weight ratio of 1:2 and dissolved in dichlorobenzene at a concentration of 24 mg mL⁻¹. Camphoric anhydride was mixed into the solution at a weight ratio of 15% to improve charge dissociation.^[33] In addition, 1,8-diiodooctane was added at a volume ratio of 3%. Next, the blend solution was heated to 70 °C and stirred overnight. The BHJ solution was passed through a 0.45 μm polytetrafluoroethylene filter before use. The ZnO layer was prepared from a precursor solution formulated^[46] by dissolving zinc acetate in a mixture of ethanolamine and 2-methoxyethanol. The ZnO precursor was stirred for 3 h before use.

Device Fabrication: The glass substrates with ITO showed a sheet resistance of $\approx 15 \Omega \text{ sq}^{-1}$. They were cleaned by sonication in 10 min steps, in a sequence of detergent, deionized water, acetone, and isopropanol. The ZnO layer was deposited by spin-coating the ZnO precursor onto the ITO substrates, followed by annealing at 400 °C for 20 min in air. The thickness for the ZnO layer was $\approx 40 \text{ nm}$. The SWIR BHJ layer was prepared by spin-coating the blend solution in a nitrogen glovebox to form films with a thickness of $\approx 100 \text{ nm}$. Then, the samples were transferred into a vacuum chamber to sequentially deposit the MoO₃, NPB, Alq₃, and LiF layers through thermal evaporation. The active area of a completed device was either 0.1 or 2 cm², as defined by the evaporation shadow mask. All the devices were encapsulated with glass cover slips and placed under white light for 5 min to passivate deep trap states and reach steady-state performance.

Device Characterization: All the devices were characterized in ambient conditions. The spectral photoresponse was measured under a monochromatic light source modulated at 315 Hz by an optical chopper. The device current was first amplified through a preamplifier (SRS 570) and then measured by a lock-in amplifier (SRS 510). For characterization at a fixed wavelength, the light source was a 1050 nm LED (Thorlabs LED1050L). The light intensity was calibrated by using a

Ge detector (Newport 818IR/DB). The bias to the device was supplied by an electrometer (Keithley 2400). The transient photoresponse was measured under a 940 nm LED (Thorlabs LED940E) modulated at different frequencies. The photocurrent was amplified by a preamplifier (SRS 570) and then recorded by an oscilloscope (RIGOL DS1054).

The photocurrent I_{photo} is obtained as the difference between the device current under illumination I_{light} and the current measured in the dark I_{dark} : $I_{\text{photo}} = I_{\text{light}} - I_{\text{dark}}$. The EQE of a photodetector is $\text{EQE} = R(hc/\lambda q) = (I_{\text{photo}}/P_{\text{in}})(hc/\lambda q)$, where R is the responsivity defined as the photocurrent I_{photo} divided by the power of the incident light P_{in} , h is Planck's constant, c is the speed of light, and q is the electron charge. The specific detectivity D^* is an important figure of merit to quantify the SNR and is defined as $D^* = RA^{0.5}/S_n$, where R is the responsivity (A W^{-1}), A is the photodetection area (cm^2), and S_n is the noise current spectral density ($\text{A Hz}^{-0.5}$) of the detector. The current spectra in Figure 3d and Figure S3, Supporting Information, were taken with the device connected to a preamplifier (SRS 570) and then to a spectrum analyzer (HP 89410A). The light source is a 940 nm LED modulated at 313 Hz. The light power is calibrated by a Si detector (Thorlabs DET36A).

The SWIR photon-to-visible photon upconversion efficiency $\eta_{\text{p-p}}$ was calculated from

$$\eta_{\text{p-p}} = \frac{N_{\text{emit}}}{N_{\text{incident}}} = \frac{\int (\lambda \phi_{\text{emit},\lambda} / hc) d\lambda}{P_{\text{in}} \lambda_{\text{in}} / hc} \quad (1)$$

where N_{emit} is the flux of emitted visible photons, N_{incident} is the flux of incoming SWIR photons, $\phi_{\text{emit},\lambda}$ is the intensity of visible light emitted at wavelength λ into half space.

Visible emission of the upconversion imager was measured by a Si detector (Thorlabs DET36A), and the visible light intensity was calculated by accounting for the variation in Si responsivity with respect to its absorption spectrum. The SWIR light was illuminated on the dual-readout imager at an incident angle of 45° . The SWIR light input and the visible light output were on the same ITO side of the device. A filter that passes short wavelength light below 800 nm was placed in front of the Si detector to block any reflected SWIR light (1050 nm). The spectrum of the visible light emitted by the imager was measured by a spectrometer (Ocean Optics USB2000).

Imaging Demonstrations: For Figure 4a,b, the light source for imaging blood vessels and blood flow was from a 940 nm LED array, providing a light intensity of 35 mW cm^{-2} . The participants in the hand imaging experiment had provided written consent to be the study subjects. For Figure 4d, the smog chamber was filled with smog particulates by burning incense inside the box. The SWIR light path was through the smog chamber length of 10 cm, and the light was focused by a lens to project onto the upconversion imager. The SWIR light was from a tungsten lamp coupled with filter that passes infrared light with wavelength $>1100 \text{ nm}$. The light intensity was $\approx 30 \text{ mW cm}^{-2}$.

Supporting Information

Supporting Information is available from the Wiley Online Library or from the author.

Acknowledgements

The authors N.L. and T.N.N. acknowledge support from National Science Foundation (ECCS-1839361) and Samsung Advanced Institute of Technology. Part of the work was performed at the San Diego Nanotechnology Infrastructure of UCSD, which was supported by NSF (ECCS-1542148).

Conflict of Interest

The authors declare no conflict of interest.

Author Contributions

N.L. and T.N.N. conceived the idea, designed the experiments, and analyzed the data. N.L. performed the fabrication and measurement of the devices. D.-S.L. contributed to demonstration ideas. N.E. and J.D.A. provided the SWIR polymer. All authors contributed to discussions and writing of the manuscript.

Data Availability Statement

Data available on request from the authors.

Keywords

organic semiconductors, pixel-less imaging, shortwave infrared, upconversion

Received: January 19, 2021

Published online:

- [1] A. Rogalski, in *Proceedings of SPIE*, SPIE, Bellingham, WA **2017**, p. 104330L.
- [2] O. T. Bruns, T. S. Bischof, D. K. Harris, D. Franke, Y. Shi, L. Riedemann, A. Bartelt, F. B. Jaworski, J. A. Carr, C. J. Rowlands, M. W. B. Wilson, O. Chen, H. Wei, G. W. Hwang, D. M. Montana, I. Coropceanu, O. B. Achorn, J. Kloepper, J. Heeren, P. T. C. So, D. Fukumura, K. F. Jensen, R. K. Jain, M. G. Bawendi, *Nat. Biomed. Eng.* **2017**, *1*, 0056.
- [3] F. P. G. de Arquer, A. Armin, P. Meredith, E. H. Sargent, *Nat. Rev. Mater.* **2017**, *2*, 16100.
- [4] X. Tang, M. M. Ackerman, M. Chen, P. Guyot-Sionnest, *Nat. Photonics* **2019**, *13*, 277.
- [5] T. Yokota, T. Nakamura, H. Kato, M. Mochizuki, M. Tada, M. Uchida, S. Lee, M. Koizumi, W. Yukita, A. Takimoto, T. Someya, *Nat. Electron.* **2020**, *3*, 113.
- [6] J. Kim, S. Kwon, Y. K. Kang, Y. Kim, M. Lee, K. Han, A. Facchetti, M. Kim, S. K. Park, *Sci. Adv.* **2019**, *5*, eaax8801.
- [7] J. A. Carr, T. A. Valdez, O. T. Bruns, M. G. Bawendi, *Proc. Natl. Acad. Sci. USA* **2016**, *113*, 9989.
- [8] R. Hany, M. Cremona, K. Strassel, *Sci. Technol. Adv. Mater.* **2019**, *20*, 497.
- [9] H. Ding, L. Lu, Z. Shi, D. Wang, L. Li, X. Li, Y. Ren, C. Liu, D. Cheng, H. Kim, N. C. Giebink, X. Wang, L. Yin, L. Zhao, M. Luo, X. Sheng, *Proc. Natl. Acad. Sci. U. S. A.* **2018**, *115*, 6632.
- [10] J. Chen, D. Ban, M. G. Helander, Z. H. Lu, P. Poole, *Adv. Mater.* **2010**, *22*, 4900.
- [11] W. Zhou, Y. Shang, F. P. G. de Arquer, K. Xu, R. Wang, S. Luo, X. Xiao, S. Zhou, R. Huang, E. H. Sargent, Z. Ning, *Nat. Electron.* **2020**, *3*, 251.
- [12] H. Yu, D. Kim, J. Lee, S. Baek, J. Lee, R. Singh, F. So, *Nat. Photonics* **2016**, *10*, 129.
- [13] N. Li, Z. Lan, Y. S. Lau, J. Xie, D. Zhao, F. Zhu, *Adv. Sci.* **2020**, *7*, 2000444.
- [14] S. W. Liu, C. C. Lee, C. H. Yuan, W. C. Su, S. Y. Lin, W. C. Chang, B. Y. Huang, C. F. Lin, Y. Z. Lee, T. H. Su, K. T. Chen, *Adv. Mater.* **2015**, *27*, 1217.
- [15] H. Tachibana, N. Aizawa, Y. Hidaka, T. Yasuda, *ACS Photonics* **2017**, *4*, 223.
- [16] D. Yang, X. Zhou, D. Ma, A. Vadim, T. Ahamad, S. M. Alshehri, *Mater. Horiz.* **2018**, *5*, 874.

- [17] Q. Song, T. Lin, Z. Su, B. Chu, H. Yang, W. Li, C. S. Lee, *J. Phys. Chem. Lett.* **2018**, *9*, 6818.
- [18] N. Li, Y. S. Lau, Z. Xiao, L. Ding, F. Zhu, *Adv. Opt. Mater.* **2018**, *6*, 1801084.
- [19] B. H. Yu, Y. Cheng, M. Li, S. W. Tsang, F. So, *ACS Appl. Mater. Interfaces* **2018**, *10*, 15920.
- [20] N. Gasparini, A. Gregori, M. Salvador, M. Biele, A. Wadsworth, S. Tedde, D. Baran, I. McCulloch, C. J. Brabec, *Adv. Mater. Technol.* **2018**, *3*, 1800104.
- [21] J. Huang, J. Lee, J. Vollbrecht, V. V. Brus, A. L. Dixon, D. X. Cao, Z. Zhu, Z. Du, H. Wang, K. Cho, G. C. Bazan, T.-Q. Nguyen, *Adv. Mater.* **2020**, *32*, 1906027.
- [22] J. Han, D. Yang, D. Ma, W. Qiao, Z. Y. Wang, *Adv. Opt. Mater.* **2018**, *6*, 1800038.
- [23] Z. Wu, Y. Zhai, H. Kim, J. D. Azoulay, T. N. Ng, *Acc. Chem. Res.* **2018**, *51*, 3144.
- [24] Z. Wu, W. Yao, A. E. London, J. D. Azoulay, T. N. Ng, *Adv. Funct. Mater.* **2018**, *28*, 1800391.
- [25] Q. Li, Y. Guo, Y. Liu, *Chem. Mater.* **2019**, *31*, 6359.
- [26] C. Wang, X. Zhang, W. Hu, *Chem. Soc. Rev.* **2020**, *49*, 653.
- [27] Y. Zhai, Z. Wang, K. S. Kwon, S. Cai, D. Lipomi, T. N. Ng, *Adv. Mater.* **2020**, 2002541.
- [28] Z. Wu, W. Yao, A. E. London, J. D. Azoulay, T. N. Ng, *ACS Appl. Mater. Interfaces* **2017**, *9*, 1654.
- [29] A. Ozcan, E. McLeod, *Annu. Rev. Biomed. Eng.* **2016**, *18*, 77.
- [30] M. P. Edgar, G. M. Gibson, M. J. Padgett, *Nat. Photonics* **2019**, *13*, 13.
- [31] W. Yao, Z. Wu, E. Huang, L. Huang, A. E. London, Z. Liu, J. D. Azoulay, T. N. Ng, *ACS Appl. Electron. Mater.* **2019**, *1*, 660.
- [32] A. London, L. Huang, B. Zhang, B. Oviedo, J. Tropp, W. Yao, Z. Wu, B. Wong, T. N. Ng, J. D. Azoulay, *Polym. Chem.* **2017**, *8*, 2922.
- [33] Z. Wu, Y. Zhai, W. Yao, N. Eedugurala, S. Zhang, L. Huang, X. Gu, J. D. Azoulay, T. N. Ng, *Adv. Funct. Mater.* **2018**, *28*, 1805738.
- [34] N. Li, J. Lim, J. D. Azoulay, T. N. Ng, *J. Mater. Chem. C* **2020**, *8*, 15142.
- [35] H. Kim, Z. Wu, N. Eedugurala, J. D. Azoulay, T. N. Ng, *ACS Appl. Mater. Interfaces* **2019**, *11*, 36880.
- [36] S. Karuthedath, Y. Firdaus, R. Z. Liang, J. Gorenflot, P. M. Beaujuge, T. D. Anthopoulos, F. Laquai, *Adv. Energy Mater.* **2019**, *9*, 1901443.
- [37] J. Meyer, S. Hamwi, M. Kröger, W. Kowalsky, T. Riedl, A. Kahn, *Adv. Mater.* **2012**, *24*, 5408.
- [38] Y. Fang, A. Armin, P. Meredith, J. Huang, *Nat. Photonics* **2019**, *13*, 1.
- [39] Z. Wu, N. Li, N. Eedugurala, J. D. Azoulay, D.-S. Leem, T. N. Ng, *npj Flexible Electron.* **2020**, *4*, 6.
- [40] G. Simone, M. J. Dyson, S. C. J. Meskers, R. A. J. Janssen, G. H. Gelinck, *Adv. Funct. Mater.* **2020**, *30*, 1904205.
- [41] K. J. Baeg, M. Binda, D. Natali, M. Caironi, Y. Y. Noh, *Adv. Mater.* **2013**, *25*, 4267.
- [42] Y. Wu, K. Fukuda, T. Yokota, T. Someya, *Adv. Mater.* **2019**, *31*, 1903687.
- [43] H. Xu, J. Liu, J. Zhang, G. Zhou, N. Luo, N. Zhao, *Adv. Mater.* **2017**, *29*, 1700975.
- [44] Y. Khan, D. Han, A. Pierre, J. Ting, X. Wang, C. M. Lochner, G. Bovo, N. Yaacobi-Gross, C. Newsome, R. Wilson, A. C. Arias, *Proc. Natl. Acad. Sci. USA* **2018**, *115*, E11015.
- [45] C. Fuentes-Hernandez, W. F. Chou, T. M. Khan, L. Diniz, J. Lukens, F. A. Larrain, V. A. Rodriguez-Toro, B. Kippelen, *Science* **2020**, *370*, 698.
- [46] B. S. Ong, C. Li, Y. Li, Y. Wu, R. S. Loutfy, *J. Am. Chem. Soc.* **2007**, *129*, 2750.